MATERIALS CHEMISTRY FRONTIERS

RESEARCH ARTICLE

View Article Online
View Journal | View Issue

Cite this: *Mater. Chem. Front.*, 2025, **9**, 3149

Iron phthalocyanine assisted bifunctional oxygen electrocatalyst for high-performance and long-life rechargeable zinc–air batteries

Zubair Ahmed,[a] Jekaterina Kozlova,[b] Arvo Kikas,[b] Vambola Kisand,[b] Alexey Treshchalov,[b] Maike Käärik,[a] Jaan Leis,[a] Jaan Aruväli,[c] Kaupo Kukli[b] and Kaido Tammeveski*[a]

The development of high-performance and long-lasting rechargeable zinc–air batteries (ZABs) requires efficient and durable bifunctional oxygen electrocatalysts that can facilitate both the oxygen reduction reaction (ORR) and the oxygen evolution reaction (OER). This advancement is crucial for enhancing the overall performance and longevity of rechargeable ZABs. However, it remains highly challenging to integrate independent ORR and OER active sites into a catalyst with high bifunctional activity. Herein, we report a simple approach to design a nonprecious metal catalyst by immobilizing iron phthalocyanine (FePc) onto Ni nanoparticle-loaded porous graphene-based heterostructures (PGHS) *via* π–π interactions. Owing to these interactions the resultant FePc@Ni-PGHS catalyst synergistically facilitate the ORR and OER bifunctional electrocatalytic performance. Consequently, as an air electrode in ZAB, it achieves a peak power density of 152 mW cm^{-2}, a large specific capacity of 862 mAh g^{-1}, and stable cycling performance for 124 h. These findings emphasize its potential as a low-cost alternative to precious metal-based electrocatalysts, offering a pathway to more sustainable and efficient electrochemical energy conversion and storage technologies.

Received 5th August 2025,
Accepted 23rd August 2025

DOI: 10.1039/d5qm00589b

rsc.li/frontiers-materials

1. Introduction

The growing energy crisis and environmental concerns have driven the development of clean, efficient, and cost-effective advanced electrochemical energy conversion and storage devices such as fuel cells and metal–air batteries.[1–4] Rechargeable zinc–air batteries (ZABs), in particular, have recently gained significant attention as energy storage devices due to their higher energy density and improved safety compared to traditional rechargeable batteries.[5–7] Notably, the use of an aqueous electrolyte makes them safer and more environmentally friendly. In rechargeable ZABs two important electrochemical reactions are involved, the oxygen reduction reaction (ORR) during discharging and the oxygen evolution reaction (OER) during the charging process at the air electrodes. Both ORR and OER have sluggish kinetics, which leads to unsatisfactory battery performance.[8] Therefore, it is vital that these reactions are activated independently and maintained close to the equilibrium of the O_2/OH^- couple. Up to now, various non-precious metal bifunctional ORR/OER electrocatalysts have been explored, mainly including bimetallic transition metal *e.g.* Fe, Co, and/or Ni containing compounds and their carbon composites.[9–11] Currently, Pt-based catalysts are known to exhibit superior ORR activity, however, they are oxidized to Pt-oxides at high anodic potentials, resulting in poor electrocatalytic activity for the OER.[12,13] Conversely, the best-known Ru/Ir-based OER electrocatalysts struggle with inadequate performance for the ORR.[14,15] This makes it challenging for these precious metal-based catalysts to achieve excellent bifunctional activity for both the reactions. Furthermore, the limited availability, high cost, and poor stability of precious metal catalysts further hinder their practical application.[16–18] Consequently, many research groups are actively focusing on developing high-performance and cost-efficient bifunctional electrocatalysts for ORR and OER to enhance battery performance and advance their practical applications.[19–21]

In particular, Fe–N–C type materials, featuring Fe–N_x sites within the carbon framework, are regarded as some of the most effective non-noble metal catalysts for replacing Pt/C in ORR electrocatalysis.[22] Therefore, iron phthalocyanine (FePc) with Fe–N_4 centres has received considerable attention as an effective electrocatalyst for the ORR.[23,24] However, FePc has a planar, symmetrical molecular structure, which limits its adsorption of

[a] *Institute of Chemistry, University of Tartu, Ravila 14a, 50411 Tartu, Estonia. E-mail: kaido.tammeveski@ut.ee*
[b] *Institute of Physics, University of Tartu, W. Ostwald Str. 1, 50411 Tartu, Estonia*
[c] *Institute of Ecology and Earth Sciences, University of Tartu, Vanemuise 46, 51014 Tartu, Estonia*

O-intermediates and inhibits its catalytic activity for the ORR.[25–27] Additionally, FePc molecules have poor electrical conductivity and tend to agglomerate.[28] To address these issues, researchers have attempted to couple FePc with defective carbon materials. This method has achieved some success in effectively mediating the charge redistribution of Fe atoms in FePc and ultimately improving its ORR performance. Most reported carbon-supported multimetallic FePc-based electrocatalysts are typically prepared by pyrolysis to obtain Fe–N_x–C catalysts. However, determining the actual active sites for ORR in these materials remains challenging because of the structural fragmentation due to loss of nitrogen ligands and also transition metal aggregation occurs at elevated temperatures leading to unpredictable activities.[29,30] At the same time, these Fe–N_x catalysts cannot meet the OER requirements at the air electrode of a rechargeable ZAB.[31] To overcome these barriers, further strategies are developed such as introduction of secondary transition metal nanostructures, such as alloys, oxides, sulfides, phosphides, *etc.* into Fe–N–C materials to enhance their electrocatalytic OER activity and consequently improve their bifunctional OER/ORR activity.[32–35] This approach enhances their bifunctional oxygen electrocatalytic activity due to unique synergistic interactions arising from the inherent polarity between the different metal species. Eventually, it introduces the concept of developing hybrid catalysts by integrating ORR-active Fe–N_x moieties and OER-active nanostructures into a carbon material to enhance bifunctional ORR/OER activity. For instance, Zhang *et al.*[36] coupled phthalocyanine analogue hemin-derived Fe–N_x sites with CoFe nanoclusters within a mesoporous carbon matrix using pyrolysis method for achieving good bifunctional OER/ORR activity and excellent activities in rechargeable ZABs. Interestingly, Ding *et al.*[37] explored non-pyrolyzed carbon nanotube bridging strategy to integrate FePc-derived single Fe atoms onto NiCo nanoparticles and owing to this integration it displayed superior ZAB performance. Despite some progress that has been made in developing such a catalyst, it remains important to explore new materials with innovative methods to reduce the ORR and OER activity barrier that causes a large charging/discharging voltage gap and poor long-term cycling performance, leading to poor energy efficiency in ZABs.

Inspired by these findings, herein we established Fe–N_4 centers in close proximity with Ni nanoparticles in carbon composites, creating a well-known established synergy between the Fe/Ni in a controllable manner in a facile non-pyrolyzed approach into a FePc@Ni-PGHS hybrid material. The FePc@Ni-PGHS material is demonstrated to be a highly active bifunctional electrocatalyst for both the ORR and OER. Based on these results, a rechargeable zinc–air battery was assembled with the FePc@Ni-PGHS air electrode, which displays an impressive peak power density (P_{max}) of 152 mW cm^{-2}, large specific capacity of 862 mAh g^{-1} at 20 mA cm^{-2}, and lasting for 124 h in cycling stability test, significantly outperforming a commercial PtRu/C catalyst, which has a P_{max} of 134 mW cm^{-2}, a specific capacity of 840 mAh g^{-1}, and stability of only 28 h. Therefore, this study provides a facile approach that enables efficient bifunctional ORR/OER electrocatalysis for electrochemical energy storage and conversion devices.

2. Experimental

2.1. Material synthesis

2.1.1. Synthesis of PGHS. The porous graphene heterostructures (PGHS) were synthesized by dispersing 50 mg of multiwalled carbon nanotubes (NC3150, ≥95%, Nanocyl S.A., Belgium) and 50 mg of graphene nanoplatelets (Strem Chemicals) in 50 mL of ethanol. Afterwards, 50 mg of Basolite (Z1200, Sigma-Aldrich) was added to this solution as a pore-inducing agent and sonicated for 2 h. The solution was then transferred to a Petri dish and dried in an oven at 60 °C overnight. The dried powder was then pyrolyzed in an N_2 atmosphere at 950 °C for 1 h. Following pyrolysis, the powder was acid-washed using 1 M HCl by stirring overnight at room temperature and repeatedly washed with Milli-Q water to remove unwanted metallic impurities.

2.1.2. Synthesis of Ni-PGHS. 50 mg of nickel nitrate hexahydrate ($Ni(NO_3)_2{\cdot}6H_2O$, ≥98%, Roth) was dissolved in 50 mL of ethanol and 100 mg of PGHS synthesized in 2.1.1 was added to this solution, followed by sonication and oven drying at 60 °C. The dried powder was then pyrolyzed at 800 °C under N_2 flow and subsequently stirred overnight in 1 M HCl and washed with Milli-Q water to obtain Ni-PGHS.

2.1.3. Synthesis of FePc@Ni-PGHS. To synthesize the FePc@Ni-PGHS composite, 10 mg of iron phthalocyanine (FePc) was dispersed in 50 mL of methanol using ultrasonication. Following this, 50 mg of Ni-PGHS, prepared in a previous step, was added to the solution. The mixture was sonicated for 2 h to facilitate the coupling of FePc molecules with the Ni-loaded porous graphene heterostructures through π–π interactions. Finally, the FePc@Ni-PGHS composite was collected by washing with vacuum filtration using Milli-Q water, followed by vacuum oven drying at 60 °C.

2.2. Material characterizations

X-ray diffraction (XRD) analysis was conducted using a Bruker D8 Advance diffractometer equipped with LYNXEYE XE-T detector and Cu Kα radiation (λ = 1.54 Å) X-ray source. Micro-Raman spectra were obtained using a Renishaw spectrometer in backscattering geometry, combined with a confocal microscope (Leica Microsystems CMS GmbH) with a 50× objective and an argon ion laser operating at 514.5 nm. The N_2 adsorption–desorption isotherms of the samples were measured using a Quantachrome NOVAtouch LX2 instrument. The specific surface area was estimated using the Brunauer–Emmett–Teller (BET) theory within the P/P_0 range of 0.02–0.2. The pore size distribution (PSD) was calculated using the quenched solid density functional theory (QSDFT) model for slit-type pores. To investigate surface morphology, Helios NanoLab 600 (FEI) was used for scanning electron microscopy (SEM). A detailed inspection of the morphological features was conducted using scanning transmission electron microscopy (STEM) with a Titan Themis 200 (FEI) instrument. Both bright field (BF) and high-angle annular dark field (HAADF) images of the sample were captured at an accelerating voltage of 200 kV. Elemental mapping in STEM was performed using a four-quadrant Super-X energy-dispersive X-ray spectroscopy (EDX) system (FEI/

Bruker). The surface elemental composition of the samples was analyzed with an INCA Energy 350 EDX spectrometer (Oxford Instruments) in a Helios NanoLab 600 SEM. The elemental composition and states were analyzed by X-ray photoelectron spectroscopy (XPS) analysis using an electron energy analyzer (SCIENTA SES-100) with Mg Kα radiation (1253.6 eV) from a nonmonochromatic twin anode X-ray tube Thermo XR3E2. The XPS binding energy was calibrated with respect to the C 1s peak and fitted with Lorentzian-Gaussian peak functions and mixture of linear and Shirley backgrounds using the Casa XPS software.

2.3. Electrochemical measurements

All electrochemical tests for the ORR and OER were conducted in a three-electrode setup under ambient conditions in O_2-saturated 0.1 M KOH electrolyte solution, utilizing a Metrohm Autolab potentiostat/galvanostat PGSTAT30. The saturated calomel electrode (SCE) connected *via* a salt bridge was employed as the reference electrode and a graphitic rod functioned as the counter electrode. Rotating disc electrode (RDE) and rotating ring-disc electrode (RRDE) served as the working electrodes with geometric areas of 0.196 and 0.164 cm^2, respectively. For RDE measurements, CTV101 (Radiometer) was used as a speed control unit, and for RRDE measurements, an AFMSRX rotator with an MSRX speed controller from Pine Research was utilized. The potentials were referenced to a reversible hydrogen electrode (RHE) using the following equation: $E_{RHE} = E_{SCE} + 0.241\ V + 0.059\ V \times pH$.

To prepare the working electrode, 2 mg of catalyst material was dispersed in 495 μL of isopropanol, along with 5 μL of a 5 wt% Nafion ionomer solution (Sigma-Aldrich). The catalyst ink was sonicated until a uniform dispersion was achieved. Then, the prepared ink was pipetted onto a cleaned glassy carbon surface and dried in an oven at 60 °C to achieve a catalyst loading of 0.2 mg cm^{-2}. Following a similar procedure, Pt/C (20 wt% Sigma-Aldrich) and RuO_2 (99% Alfa Aesar) coated electrodes were prepared with a catalyst loading of 0.1 mg cm^{-2}. The ORR polarization curves were recorded from 1.1 to 0 V *vs.* RHE at a scan rate (ν) of 10 mV s^{-1} at rotation speeds (ω) ranging from 600 to 3000 rpm. The Koutecky–Levich (K–L) analysis for O_2 reduction data is detailed in SI. The percentage yield of peroxide formation (%HO_2^-) and the electron transfer number (n) in the ORR process were calculated using eqn (1) and (2), respectively.[38,39]

$$HO_2^-\ (\%) = \frac{200 \times \frac{|I_r|}{N}}{|I_{disk}| + \frac{|I_r|}{N}} \quad (1)$$

$$n = \frac{4|I_d|}{|I_d| + \frac{|I_r|}{N}} \quad (2)$$

where I_d refers to the disk current, I_r is the ring current, and N is the current collection efficiency of the platinum (Pt) ring ($N = 0.25$). The Pt ring electrode of the RRDE tip was maintained at a potential of 1.55 V *vs.* RHE and was activated before each measurement.

The OER polarization curves were recorded within a potential range from 1.2 to 1.8 V *vs.* RHE at 1600 rpm with 10 mV s^{-1} of scan rate. Before electrochemical measurements, the electrodes were activated by performing 20 fast scans within the same potential window. Additionally, *iR* correction was applied to the polarization curves using Nova 2.1 software. Electrochemical impedance spectroscopy (EIS) measurements were done in the frequency range from 100 kHz to 0.1 kHz with an amplitude of 0.01 V at 0.8 V *vs.* RHE for ORR and at 1.65 V *vs.* RHE for OER. To evaluate the double-layer capacitance (C_{dl}), cyclic voltammograms (CV) were recorded in the non-faradaic region (1.08 to 1.18 V *vs.* RHE) at various scan rates (10, 20, 30, 40, 50, 60, and 100 mV s^{-1}). C_{dl} is then calculated from the slope of $\Delta j/2$ ($\Delta j = j_{anodic} - j_{cathodic}$) *vs.* scan rate plot.

2.4. Zn–air battery (ZAB) assembly

In-house liquid-state ZABs were constructed using the same setup as in the previous investigation.[40,41] An aqueous solution of 6 M potassium hydroxide (KOH) containing 0.2 M zinc acetate (98%, Fisher Scientific) as the electrolyte and is paired with a 0.2 mm thick zinc plate (99.9%, Auto-plaza). For the air electrode, a catalyst-coated gas diffusion layer (GDL, Sigracet BB39) measuring 1.8 cm × 1.8 cm with a Ni mesh serving as the current collector. To prepare the air electrode, 10 mg of catalyst was dispersed in 1000 μL (200 μL of water and 800 μL of ethanol) with an additional 20 μL of a 5% Nafion solution to the ink and sonicated until a homogenous dispersion is formed. The ink was then drop-casted onto GDL to obtain 2 mg cm^{-2} of catalyst loading and oven dried at 60 °C. For comparison, the commercial PtRu/C (50% Pt: 25% Ru: 25% C; Alfa Aesar) catalyst electrode was prepared using the same method but with a catalyst loading of 1 mg cm^{-2}. At the air electrode, the catalyst area exposed to the electrolyte solution is 0.79 cm^2. Specific capacity was calculated at a discharge current density of 20 mA cm^{-2} with respect to the Zn weight loss. Stability was evaluated through charge–discharge cycling at 5 mA cm^{-2}, with each cycle lasting 10 min. The calculation for specific capacity and round-trip efficiency is detailed in the SI. The EIS measurements for the ZAB were conducted at a discharging potential of 1.25 V in a frequency range from 100 kHz to 0.1 kHz and an amplitude of 0.01 V.

3. Results and discussion

3.1. Physical characterization of electrocatalysts

As illustrated in Scheme 1, nanocarbon composites were first prepared in this process by annealing carbon nanotubes with graphene nanoplatelets in the presence of Zn-containing basolite at 950 °C to obtain porous graphene-based heterostructure (PGHS).

This composite is beneficial in exposing more active sites to enhance the electron transfer and mass transfer during the electrocatalytic process. Next, Ni nanoparticles were grown into the heterostructured nanocarbon matrix *via* pyrolyzing method using nickel nitrate hexahydrate and the prepared PGHS support in an inert atmosphere at 800 °C to get Ni-PGHS. This step is followed by the immobilization of iron phthalocyanine (FePc) within Ni-containing graphene-based heterostructures through

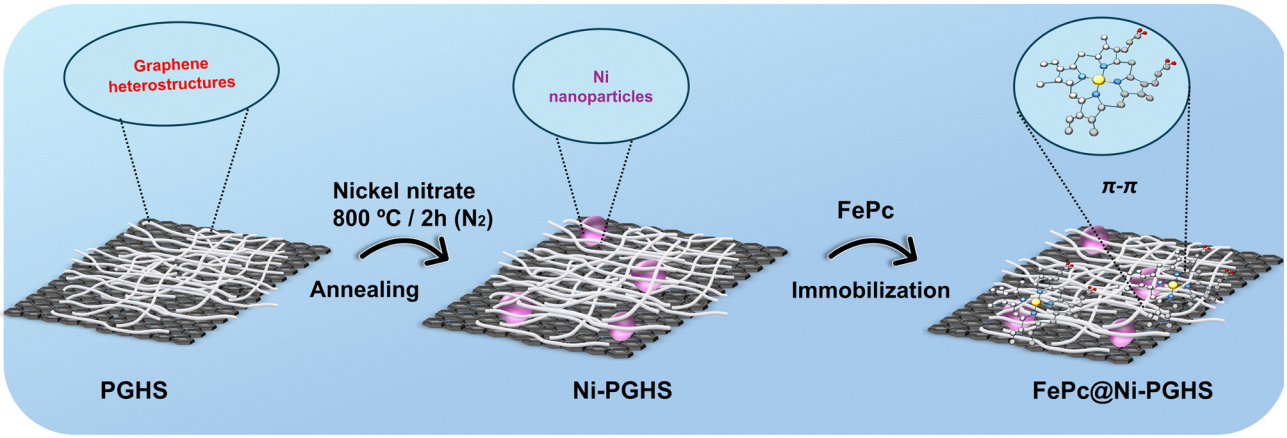

Scheme 1 The synthesis route for preparing FePc@Ni-PGHS as bifunctional ORR/OER electrocatalysts.

π–π interactions leading to the formation of the final product named FePc@Ni-PGHS.

The X-ray diffraction (XRD) measurement was performed to reveal the crystallographic structure of the prepared materials shown in Fig. 1(a). The XRD patterns of the nanocarbon-based PGHS catalyst showed a distinctive peak at *ca.* 25.6°, consistent to the reflections of the graphitic carbon planes (002). In the XRD patterns of Ni-PGHS the peaks observed at 44.5°, 51.8°, and 76.4° match well with the face-centered cubic structure of metallic Ni (PDF-#04-0850) assigned to its (111), (200), and (220) planes, respectively. While two relatively weak peaks at 6.9° and 15.4° assigned to FePc in the FePc@Ni-PGHS material, suggest that FePc is effectively anchored to the substrate. In the Raman spectroscopy analysis, the FePc@Ni-PGHS material exhibits signature vibrational peaks of FePc (Fig. S1), further confirming that FePc is successfully integrated into FePc@Ni-PGHS.[42]

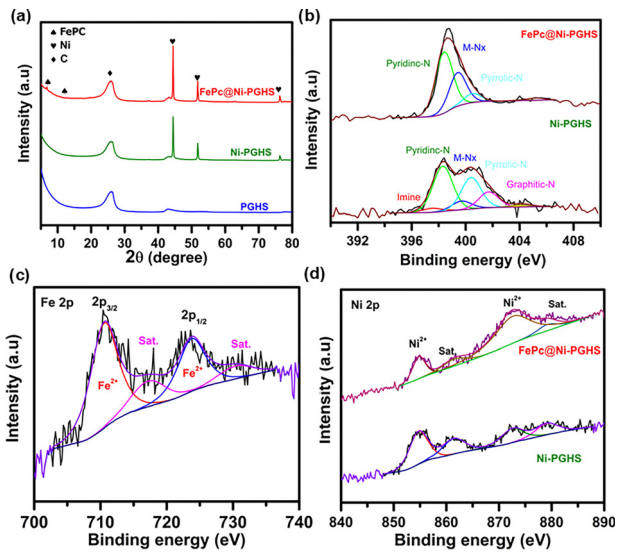

Fig. 1 (a) XRD patterns of the prepared materials. The deconvoluted XPS spectra of (b) N 1s of FePc@Ni-PGHS and Ni-PGHS, (c) Fe 2p of FePc@Ni-PGHS, and (d) Ni 2p of FePc@Ni-PGHS and Ni-PGHS.

To investigate the chemical composition and the valence state of Fe and Ni species in the FePc@Ni-PGHS material, the X-ray photoelectron spectroscopy (XPS) was measured. The XPS survey spectrum (Fig. S2) indicates the coexistence of constituent elements such as Fe, Ni, C, N, and O in the corresponding material. The prepared catalyst materials contained a variety of nitrogen moieties. These N species include pyridinic nitrogen (~398 eV), pyrrolic nitrogen (~400 eV), nitrogen-coordinated metal centers (M–N_x, ~399 eV), imines (~397.5 eV), graphitic nitrogen (~401 eV), and oxidized nitrogen (N–O, ~404 eV) in Ni-PGHS.[43] While FePc@Ni-PGHS shows rich pyridinic-N (398.4 eV), M–N_x (399.3 eV), and pyrrolic-N (400.2 eV) functionalities, which likely originate from the FePc molecules (Fig. 1(b)).[44] The well-defined Fe–N_4 sites in FePc play a crucial role in the kinetics of the ORR due to its local coordination environment.[45] The high-resolution Fe 2p XPS spectrum (Fig. 1(c)) shows two major peaks at 710.5 eV ($2p_{3/2}$) and 725.1 eV ($2p_{1/2}$) along with a minor shakeup satellite, which indicate that Fe element exists as Fe–N_x species, illustrating that FePc structure remains intact in FePc@Ni-PGHS.[46] By comparing the high-resolution Ni 2p XPS spectrum (Fig. 1(d)), in FePc@Ni-PGHS the Ni^{2+} was identified by the Ni $2p_{3/2}$ (854.7 eV) and Ni $2p_{1/2}$ (873.1 eV) peaks with two satellites at 861.3 and 879.9 eV.[47,48] Notably, the XPS peaks of Ni 2p show a slight shift to higher binding energy after the introduction of FePc, illustrating the electronic interaction with Fe in FePc@Ni-PGHS. These electronic interactions between Fe and Ni facilitate a non-uniform charge distribution, leading to enhanced OER kinetics.[49]

The surface morphology of the prepared catalysts was initially examined using scanning electron microscopy (SEM). Fig. S3a and b shows that the FePc@Ni-PGHS features a Fe/Ni-modified porous carbon support of CNTs wrapped around graphene nanoplatelets forming a 3-D crosslink network. These porous CNT/graphene nanoplatelet heterostructures are also visible in Ni-PGHS (Fig. S3c and d) and PGHS (Fig. S3e and f), which is favorable for better activity, stability, and large number of active sites in electrocatalysis.[50] Furthermore, the bulk elemental composition of the prepared catalysts was examined using the SEM-EDX (Table S1). The FePc@Ni-PGHS contained approximately 0.90 wt% Fe and 5.04 wt.% Ni, which closely matched the

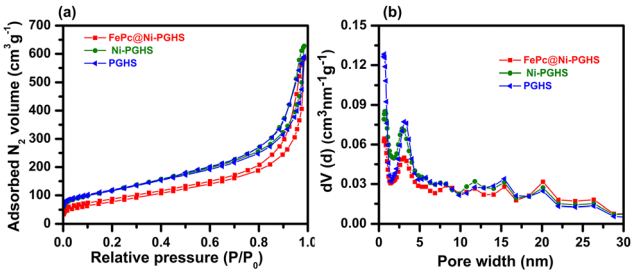

Fig. 2 (a) N_2 adsorption–desorption isotherms and (b) pore size distribution of the FePc@Ni-PGHS, Ni-PGHS, and PGHS samples.

amounts of metals added during synthesis. The specific surface area and pore size distribution of the prepared materials were analyzed using N_2 adsorption–desorption isotherms, as the porous structure of the catalyst facilitate electron and ion transport through the channels and affects the overall electrocatalytic performance.[51,52] The PGHS material demonstrated a high surface area (S_{dft}) of 412 m^2 g^{-1} (Fig. 2(a)). This feature opens the freeway for exposing more active sites at the catalyst/electrolyte interface, which accelerates electron transfer and mass-transfer during electrocatalysis. It also stabilizes the dopant atoms and prevents their aggregation, making it an excellent support material for enhancing the performance of the electrocatalyst. The Ni-PGHS and FePc@Ni-PGHS materials exhibit a slightly decreased S_{dft} of 379 and 287 m^2 g^{-1}, respectively, which could be due to the partial shrink of the carbon nanostructure caused by the introducing Ni/Fe loadings. Additionally, Fig. 2(b) indicates the mesoporous structure that FePc@Ni-PGHS. The estimated S_{dft} values of the prepared catalysts from different approaches is provided in Table S2.

This mesoporous network modifies the chemisorption of O*/OH* intermediates and lowers the overall energy barrier of ORR, while also improving durability and $4e^-$ selectivity in alkaline media, ultimately influencing the overall electrocatalytic activity.[53]

Since, SEM is limited to lower magnifications and may not provide an in-depth view of the catalyst material. Therefore, TEM was employed to further investigate the catalyst morphology and elemental distribution in more detail. Bright-field (BF) STEM images for the prepared catalysts (Fig. 3(a)) confirm the metal species modified graphene nanoplatelets homogenously wrapped with CNTs. The high resolution (HR)-STEM (Fig. 3(b)) shows the lattice spacings of 0.20 nm assigned to the

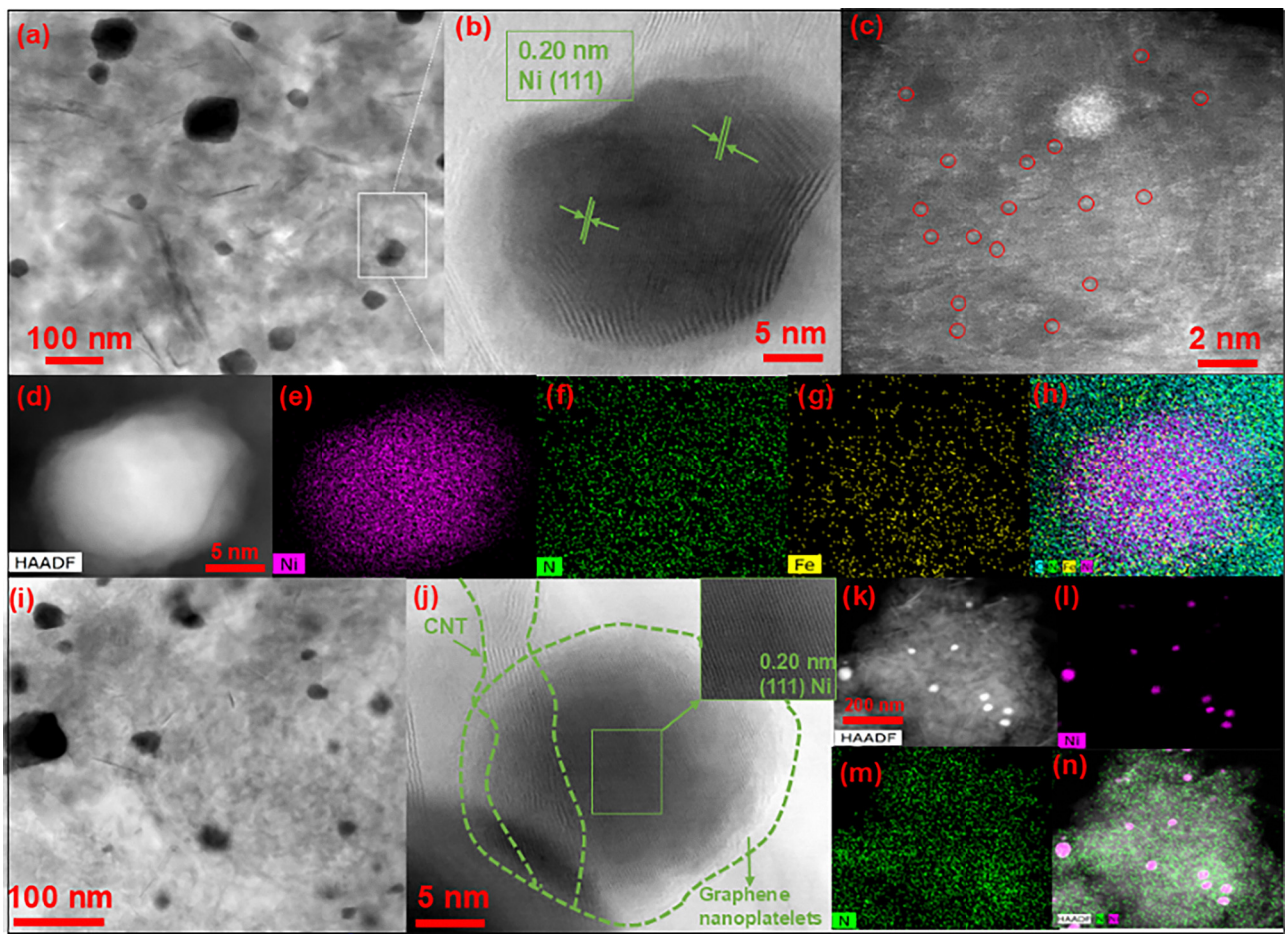

Fig. 3 (a) BF-STEM image, (b) HR-STEM image, (c) atomic-resolution HAADF-STEM image of FePc@Ni-PGHS, (d)–(h) HAADF-STEM and mapping images of FePc@Ni-PGHS. (i) BF-TEM image, (j) HR-STEM image of Ni nanoparticles wrapped in CNT/graphene nanoplatelets heterostructures, (k)–(n) HAADF-STEM image and the corresponding EDX element mappings of Ni-PGHS.

Ni(111) planes, which is in good agreement with the XRD results.

Further characterization of the FePc@Ni-PGHS material at the atomic level is performed under high annular dark-field TEM (HAADF-STEM) imaging. The abundant isolated bright spots originating from the *Z*-contrast imaging between metal atoms and carbon substrate indicate the presence of isolated Fe atoms anchored on a graphene substrate (Fig. 3(c)).

Furthermore, STEM-EDX elemental mapping (Fig. 3(d) and (h)) show the homogeneous distribution of constituent elements in the FePc@Ni-PGHS and verify that Fe exists primarily as single atoms, while Ni is dispersed as nanoparticles. Likewise, FePc@Ni-PGHS, the STEM image of Ni-PGHS (Fig. 3(i)) also presents the typical crystalline Ni trapped in a graphitic carbon shell with the unchanged lattice spacing of 0.20 nm (Fig. 3(j)). The consistent lattice spacing in the FePc@Ni-PGHS and Ni-PGHS demonstrate that FePc do not alter the Ni crystal structure and the interaction between FePc and Ni-PGHS occur through π–π stacking. The acquired elemental maps of Ni-PGHS are shown in Fig. 3(k)–(n).

3.2. Electrocatalytic performance for ORR and OER

Fig. S4 depicted the CV profiles of FePc@Ni-PGHS recorded at a scan rate of 50 mV s^{-1} in both Ar and O_2-saturated 0.1 M KOH electrolyte. The CV peak is absent in an Ar-saturated solution for FePc@Ni-PGHS. In contrast, a well-defined cathodic peak is observed at 0.90 V in the O_2-saturated solution, confirming its ORR activity. As indicated by the RDE polarization curves at 1600 rpm (Fig. 4(a)), FePc@Ni-PGHS demonstrates the highest ORR activity among the examined catalysts in terms of the onset potential (E_{onset}), half-wave potential ($E_{1/2}$), and limiting current density (j_L) values. The FePc@Ni-PGHS catalyst displays a high $E_{1/2}$ of 0.90 V, E_{onset} of 0.96 V *vs.* RHE, and a j_L of 6.30 mA cm^{-2} at 1600 rpm, which surpasses the commercial Pt/C (20 wt%) catalyst with $E_{1/2}$ = 0.838 V, E_{onset} = 0.99 V, and j_L = 5.99 mA cm^{-2}. The Tafel slope value obtained from the corresponding LSV curves for all the catalysts are presented in Fig. 4(b). The FePc@Ni-PGHS display a low Tafel slope of −38 mV dec^{-1} as compared to that of Ni-PGHS (−86 mV dec^{-1}), PGHS (−83 mV dec^{-1}), and Pt/C (−86 mV dec^{-1}), indicating desirable ORR kinetics of FePc@Ni-PGHS. The EIS measurements

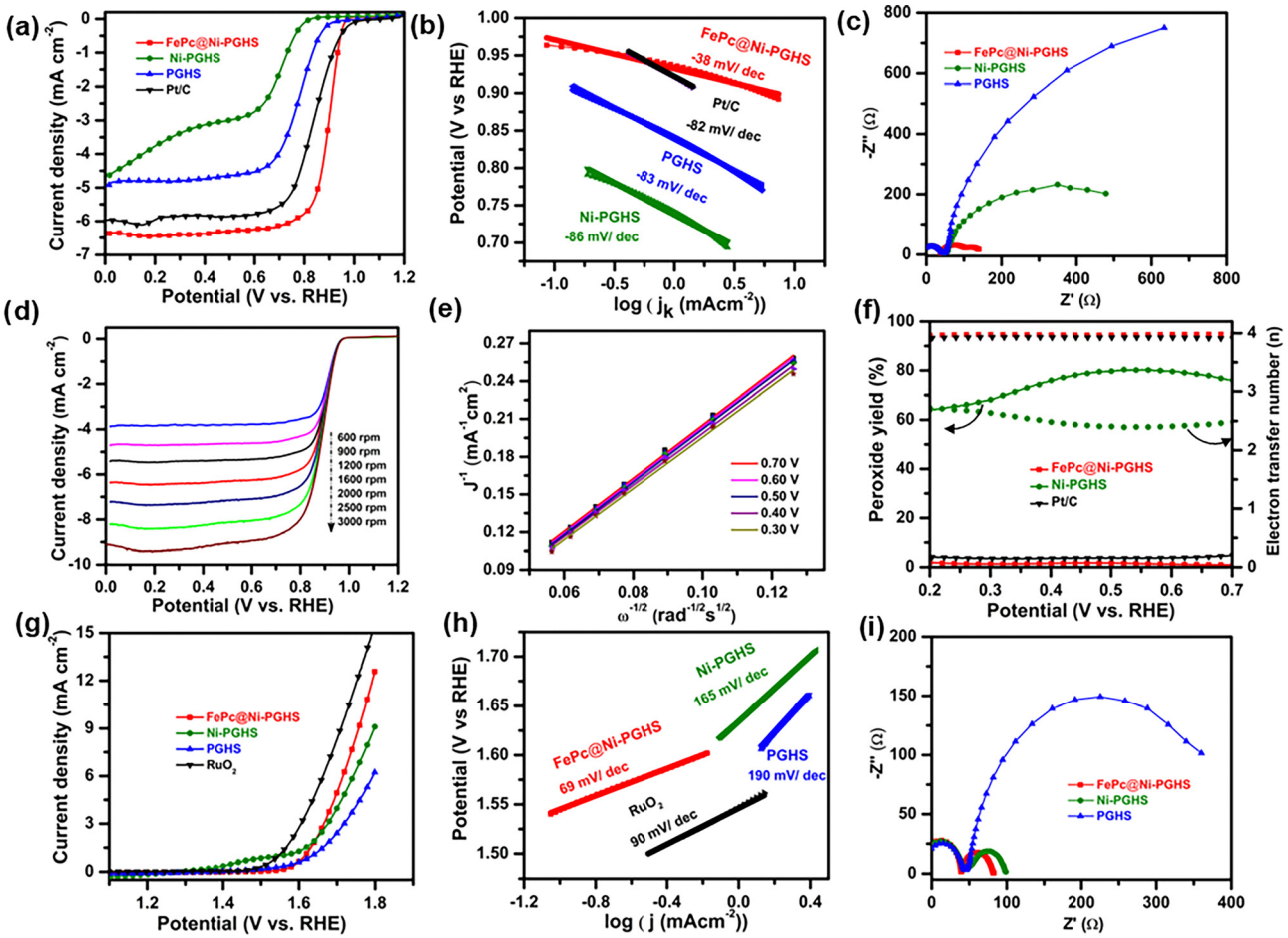

Fig. 4 Electrochemical performances. (a) LSV curves in O_2-saturated 0.1 M KOH solution at 1600 rpm and 10 mV s^{-1}, (b) Tafel plots for the ORR derived from (a), and (c) EIS spectra of FePc@Ni-PGHS, Ni-PGHS, and PGHS catalysts recorded at 0.80 V *vs.* RHE. (d) LSV curves at different rotation speeds and (e) K–L plots for FePc@Ni-PGHS. (f) Electron transfer number (*n*) and the HO_2^- yield of the examined catalysts. (g) OER polarization curves at a scan rate of 10 mV s^{-1} in 0.1 M KOH electrolyte, (h) Tafel pots for the OER, and (i) EIS spectra of FePc@Ni-PGHS, Ni-PGHS, and PGHS catalysts recorded at 1.65 V *vs.* RHE.

were further used to evaluate their catalytic kinetics. As depicted in Fig. 4(c), the first semicircle that appears at high frequency is not a true semicircle and might be influenced by parasitic inductance, contact resistance, or the instrument. While the semicircle appears at a lower frequency fits well in the Randles circuit, which consists of the solution resistance (R_s) in series with a parallel combination of a resistor (R_{ct}) and a constant phase element (CPE). The CPE models the behavior of a double layer, which deviates from an ideal capacitor and can be correlated with the surface properties of the catalyst. While, the value of R_{ct} is a function of potential and varies inversely to electrocatalytic performance. Here, the rising arc from the high-frequency region of the semicircle shows a double-layer capacitor starting to build up, showing both resistive and capacitive behaviour.[54,55] The improved ORR kinetics of FePc@Ni-PGHS is also evidenced by a lower charge transfer resistance compared to other investigated catalysts. The EIS fitting parameters and the circuit diagram is provided in Table S3 and Fig. S5, respectively.

The ORR pathway of the prepared catalysts is analyzed by the RDE polarization curves recorded at varying rotation rates in O_2-saturated 0.1 M KOH electrolyte (Fig. 4(d) and Fig. S6). The corresponding Koutecky–Levich (K–L) plots are shown in Fig. 4(e) and Fig. S7. The linear K–L plots indicate that FePc@Ni-PGHS demonstrate the first-order kinetics toward dissolved O_2 concentration and similar electron transfer number (n) during the ORR process (Fig. 4(e)). The average n value obtained from the slope of the K–L plots is *ca.* 3.98, indicating the favorable $4e^-$ ORR process of the FePc@Ni-PGHS. Furthermore, the HO_2^- yield and the n values were calculated based on the RRDE voltammograms. As shown in Fig. 4(f), the calculated HO_2^- yield of FePc@Ni-PGHS is below 5% with n nearly equivalent to 4, indicating the most preferred $4e^-$ reduction of O_2 to OH^-, consistent with the n value obtained from the K–L analysis. The ring current of the examined catalysts is presented in Fig. S8, where FePc@Ni-PGHS exhibited a lower ring current compared to the other catalysts. Specifically, FePc in the low and high spin states may have unoccupied 3d orbitals, while a single d_{z^2} electron in the intermediate spin state is easily available to penetrate antibonding π-orbitals of the O_2 molecule. These factors optimize the binding strength of the intermediates generated in the ORR, thus causing enhanced ORR activity.[56] In order to assess the influence of the different sites involved in the ORR process, the ORR polarization curves were recorded in NaCN-free and 10 mM NaCN containing 0.1 M KOH electrolyte solution. Since Fe–N_4 moiety in FePc presents a square planar geometry, cyanide ions are capable to block these sites for O_2 reduction forming a stable adduct and causing a decrease in the ORR performance of the catalyst material.[57–59] A substantial decrease in the ORR activity is observed, indicated by a negative shift in the half-wave potential ($\Delta E_{1/2}$ = 240 mV) for FePc@Ni-PGHS (Fig. S9). This suggests that the ORR activity associated with FePc in FePc@Ni-PGHS is suppressed by the NaCN addition, indicating its significant role of the Fe–N_4 sites in the enhanced ORR activity. Meanwhile, the remaining electrocatalytic ORR activity can be attributed to the Ni nanoparticles and N-doped nanocarbon matrix. The OER is crucial during the charging processes of the rechargeable Zn–air battery. The OER polarization curves of FePc@Ni-PGHS and other investigated materials are shown in Fig. 4(g). FePc@Ni-PGHS with an OER potential (E_{j10}, determined at the OER current density of 10 mA cm^{-2}) of 1.76 V, outperforms all other studied catalysts and is comparable to commercial RuO_2 (E_{j10} = 1.72 V).

In the OER mechanism in alkaline media on the Ni catalysts the real active center is the oxides/hydroxides generated on the surface.[60] However, NiO has a strong OH* adsorption energy, which lowers its OER efficiency. It is well established that the Ni–Fe synergistic interaction increase the Ni valence through Fe doping that further increases the OER activity. The Tafel slope obtained from the OER polarization curve of FePc@Ni-PGHS is 69 mV dec^{-1}, which is lower than that of Ni-PGHS (165 mV dec^{-1}), PGHS (190 mV dec^{-1}), and RuO_2 (90 mV dec^{-1}) reflecting fast OER kinetics of FePc@Ni-PGHS (Fig. 4(h)). Additionally, FePc@Ni-PGHS displays a smaller charge transfer resistance compared to Ni-PGHS in the Nyquist plot (Fig. 4(i)). This lower resistance supports the improved OER kinetics, attributed to integration of Ni nanoparticles and FePc in the FePc@Ni-PGHS catalyst. The EIS fitting parameters and the circuit diagram is provided in Table S4 and Fig. S10, respectively. The electrochemically active surface area (ECSA) of the prepared catalysts were analyzed based on the double-layer capacitances (C_{dl}). C_{dl} is evaluated from the slope of the linear lines obtained by plotting the difference in double layer charging current between anodic and cathodic CV scans in a non-faradaic region against the scan rates. The C_{dl} values are 5.6, 3.2, and 2.4 mF cm^{-2} for FePc@Ni-PGHS, Ni-PGHS, and PGHS, respectively, demonstrating favorable electrode/electrolyte interface with higher number of active sites in the FePc@Ni-PGHS catalyst (Fig. S11). In addition, the E_{onset}, $E_{1/2}$, j_L, and E_{j10} values of all the prepared materials along with Pt/C and RuO_2 are tabulated in Table S5. The bifunctional OER/ORR activity is mainly assessed based on the potential gap ($\Delta E = E_{j10} - E_{1/2}$) as a key indicator of the bifunctional activity. The smaller the ΔE value, the better the bifunctional OER/ORR activity. As shown in Fig. S12 the FePc@Ni-PGHS gives a decent ΔE of 0.86 V, better than that of Pt/C/RuO_2 catalysts (ΔE = 0.89 V) and is competitive with some of the recently reported bifunctional OER/ORR electrocatalysts (Table S6). Therefore, FePc@Ni-PGHS exhibits a good bifunctional ORR/OER activity, verifying the advantage of the interface engineering of the FePc in the Ni-PGHS that leads to efficient electrocatalysts with high activity and selectivity.

3.3. Zn–air battery performance

Based on the bifunctional oxygen electrocatalytic activity for the investigated catalysts, a homemade rechargeable liquid zinc–air battery was assembled (Fig. 5(a)) to explore the practical application prospect. The FePc@Ni-PGHS catalyst coated on a gas diffusion layer (GDL) employed as an air electrode and assembled and tested in ZAB. For comparison, Ni-PGHS and PtRu/C catalysts are also assessed and tested under similar conditions. The ZAB with FePc@Ni-PGHS possesses a higher open-circuit voltage (OCV) of 1.46 V, close to that of the PtRu/C-based ZAB (1.47 V). Fig. 5(b) shows the peak power density of

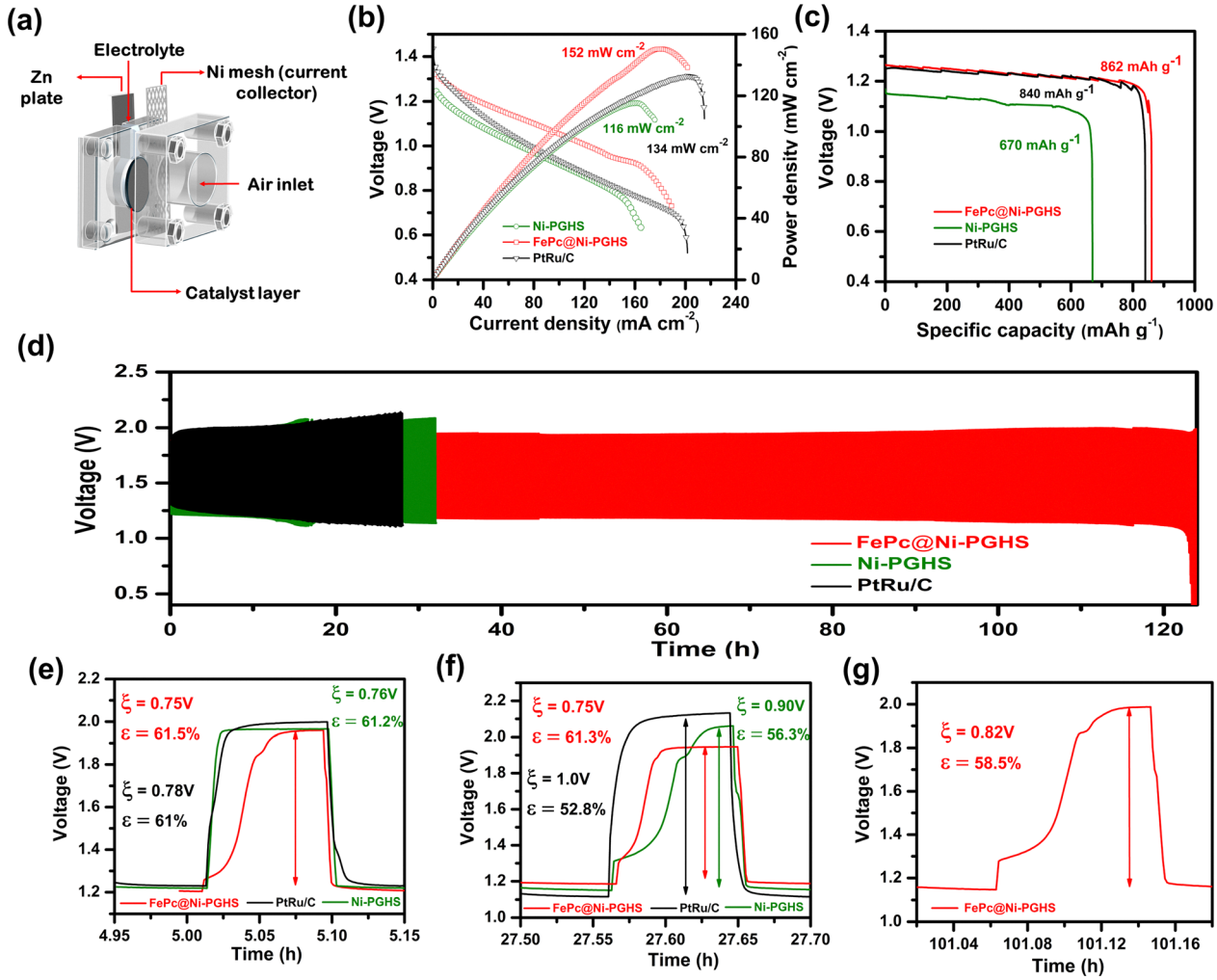

Fig. 5 (a) Schematic illustration of liquid Zn–air battery set-up using 6 M KOH with 0.2 M zinc acetate as electrolyte. (b) Polarization and power density curves, (c) Zn mass-normalized specific capacity at 20 mA cm^{-2}, and (d) Galvanostatic long-term charge–discharge of rechargeable ZABs with FePc@Ni-PGHS, Ni-PGHS, and PGHS air electrode at 5 mA cm^{-2} current density (5 min charging and 5 min discharging). (e)–(g) Voltage gap and round-trip energy efficiencies at different time periods of examined catalysts.

the FePc@Ni-PGHS driven ZAB is 152 mW cm^{-2}, higher than that of the ZAB fabricated with Ni-PGHS (116 mW cm^{-2}) and PtRu/C (134 mW cm^{-2}) air electrodes. Additionally, the specific capacity of the catalysts is assessed through the galvanostatic discharge at a current density of 20 mA cm^{-2} (Fig. 5(c)). Based upon the zinc consumption during discharge, the FePc@Ni-PGHS displays a specific capacity of 862 mAh g^{-1}, exceeding those of the Ni-PGHS (670 mAh g^{-1}) and PtRu/C (840 mAh g^{-1}) driven zinc–air batteries. This evaluation illustrates the superior rate performance and therefore, output performance of FePc@Ni-PGHS. Altogether, FePc@Ni-PGHS as air electrode displays highly competitive ZAB performance compared with many recent reports on non-precious metal-based catalysts (Table S7). Apart from the ZAB output performance, the durability of the catalysts employed as air electrodes in ZAB was assessed by means of constant current charge–discharge cycles at 5 mA cm^{-2} current density. As depicted in Fig. 5(d), the FePc@Ni-PGHS catalyst-based ZAB delivers a stable operation for around 124 h. In comparison, the PtRu/C and Ni-PGHS batteries lasted only 28 and 60 h, respectively. The PtRu/C based ZAB exhibits a significantly faster degradation rate than other investigated air electrodes (*i.e.* FePc@Ni-PGHS and Ni-PGHS). This is attributed to the higher current density in PtRu/C catalyst, leading to severe carbon corrosion resulting in the electrode flooding during long-term testing, and the oxidation and dissolution of Pt/Ru nanoparticles.[61,62] More specifically, for the initial cycle, FePc@Ni-PGHS delivers a narrower voltage gap (ξ) of 0.75 V, which is lower than that of Ni-PGHS (ξ = 0.76 V) and PtRu/C (ξ = 0.78 V) with better round-trip efficiency (ε) of 61.5% slightly higher than that of Ni-PGHS (61.2%) and PtRu/C (61%) (Fig. 5(e)). In particular, the smaller charge–discharge voltage gap of FePc@Ni-PGHS reveals its superior rechargeability and roundtrip efficiency. Furthermore, after 27 h, the FePc@Ni-PGHS remain relatively stable with ξ = 0.75 V and ε = 61.3%, whereas PtRu/C shows a significant decrease in electrocatalytic activity with increased charge–discharge voltage gap (ξ = 1.0 V) and a reduced round-trip efficiency of 52.8% (Fig. 5(f)). A noticeable decline in

performance was also observed for Ni-PGHS, which experienced high charging and discharging voltages with ξ = 0.90 V and a reduced round-trip efficiency of 56.3%, (Fig. 5(f)). In contrast, as presented in Fig. 5(g), the ZAB assembled with FePc@Ni-PGHS maintains stable electrocatalytic behavior for over 100 h, showing only a slight increase in voltage gap (ξ = 0.82 V) and reduced round-trip efficiency of ε = 58.5%. The excellent cycling stability of FePc@Ni-PGHS within the rechargeable ZAB operating environments suggests that the FePc@Ni-PGHS catalyst layer is not hindered by dissolved zinc ions, thereby maintaining its stable performance. The changes in the FePc@Ni-PGHS air electrode were analyzed using the EIS measurements conducted both before and after stability tests. As shown in Fig. S13, the FePc@Ni-PGHS-based ZAB exhibited a slight increase in the charge transfer resistance following the stability tests. This increase may be due to carbon corrosion occurring in the catalyst or in the used GDL. It is important to note that the ZAB performance can be significantly improved by adjusting battery parameters, such as mechanical adaptability and resilience of each component (cathode, anode, and electrolyte).[63–65] These modifications can greatly benefit the ZAB technology and boost the performance of the electrocatalysts. Therefore, the FePc@Ni-PGHS catalyst not only displays high intrinsic electrocatalytic activity and stability but also improves the overall cycle life and round-trip efficiency of the ZAB.

4. Conclusions

In summary, we utilized a simple non-pyrolyzed strategy to create interfacial contact between FePc-derived Fe–N_x moieties and Ni nanoparticles trapped within graphene-based heterostructures into a hybrid material that performs as a robust and efficient bifunctional oxygen electrocatalyst. Experimental results, including HAADF-STEM imaging and active site cyanide poisoning test, demonstrate the substantial contribution of atomic Fe–N_x sites for the ORR, which also enhances the OER performance when coupled with Ni nanoparticles embedded in graphene heterostructures in the FePc@Ni-PGHS catalyst. As a result, the FePc@Ni-PGHS catalyst displays excellent bifunctional electrocatalytic activity (ΔE = 0.86 V), outperforming a commercial Pt/C + RuO_2 catalyst (ΔE = 0.89 V). Furthermore, FePc@Ni-PGHS-based ZAB exhibits a high peak power density of 152 mW cm^{-2}, exceeding that of PtRu/C-based ZAB (134 mW cm^{-2}) with prominent specific capacity. More importantly, the ZAB with FePc@Ni-PGHS air electrode exhibits long-lasting cycling stability of 124 h in a single run at 5 mA cm^{-2}, while delivering a low charge–discharge voltage gap (0.75 V @ 5 mA cm^{-2}) and high reversibility (initial round-trip efficiency of 61.5%). Making them a competitive and environmentally friendly non-precious metal-based bifunctional oxygen electrocatalysts for sustainable green energy applications.

Author contributions

Zubair Ahmed: writing – review & editing, writing – original draft, methodology, investigation, data curation, funding acquisition, conceptualization. Jekaterina Kozlova: investigation, writing – review & editing, formal analysis. Arvo Kikas: investigation. Vambola Kisand: funding acquisition. Alexey Treshchalov: investigation, methodology. Maike Käärik: investigation. Jaan Leis: methodology, funding acquisition, writing – review & editing. Jaan Aruväli: investigation. Kaupo Kukli: methodology, funding acquisition, writing – review & editing. Kaido Tammeveski: writing – review & editing, resources, methodology, funding acquisition, conceptualization.

Conflicts of interest

There are no conflicts to declare.

Data availability

The data supporting this article have been included as part of the SI. See DOI: https://doi.org/10.1039/d5qm00589b

Acknowledgements

We sincerely acknowledge the financial support provided by the Estonian Research Council under incoming postdoctoral grant SJD67 along with personal research grants (PRG2569, PRG2594, PRG1509, and TEM-TA31). We would also like to thank the financial support provided by the Estonian Ministry of Education and Research (TK210, Centre of Excellence in Sustainable Green Hydrogen and Energy Technologies).

References

1 A. Kundu, S. Mallick, S. Ghora and C. R. Raj, Advanced Oxygen Electrocatalyst for Air-Breathing Electrode in Zn–Air Batteries, *ACS Appl. Mater. Interfaces*, 2021, **13**, 40172–40199.
2 S. Ding, J. A. Barr, Q. Shi, Y. Zeng, P. Tieu, Z. Lyu, L. Fang, T. Li, X. Pan, S. P. Beckman, D. Du, H. Lin, J.-C. Li, G. Wu and Y. Lin, Engineering Atomic Single Metal–FeN_4Cl Sites with Enhanced Oxygen-Reduction Activity for High-Performance Proton Exchange Membrane Fuel Cells, *ACS Nano*, 2022, **16**, 15165–15174.
3 S. Das, S. Bhattacharjee, S. Mondal, S. Dutta, N. Bothra, S. K. Pati and S. Bhattacharyya, Bimetallic Zero-Valent Alloy with Measured High-Valent Surface States to Reinforce the Bifunctional Activity in Rechargeable Zinc–Air Batteries, *ACS Sustainable Chem. Eng.*, 2021, **9**, 14868–14880.
4 Y. Song, L. Xia, M. Salla, S. Xi, W. Fu, W. Wang, M. Gao, S. Huang, S. Huang and X. Wang, A Hybrid Redox-Mediated Zinc–Air Fuel Cell for Scalable and Sustained Power Generation, *Angew. Chem., Int. Ed.*, 2024, **63**, e202314796.
5 Y.-P. Deng, Y. Jiang, R. Liang, N. Chen, W. Chen, Z.-W. Yin, G. King, D. Su, X. Wang and Z. Chen, Reconstructing 3d-Metal Electrocatalysts through Anionic Evolution in Zinc–Air Batteries, *J. Am. Chem. Soc.*, 2023, **145**, 20248–20260.
6 G. Li, W. Deng, L. He, J. Wu, J. Liu, T. Wu, Y. Wang and X. Wang, Zn, Co, and Fe Tridoped N–C Core–Shell

Nanocages as the High-Efficiency Oxygen Reduction Reaction Electrocatalyst in Zinc–Air Batteries, *ACS Appl. Mater. Interfaces*, 2021, **13**, 28324–28333.

7 D. Qiu, H. Wang, T. Ma, J. Huang, Z. Meng, D. Fan, C. R. Bowen, H. Lu, Y. Liu and S. Chandrasekaran, Promoting Electrocatalytic Oxygen Reactions Using Advanced Heterostructures for Rechargeable Zinc–Air Battery Applications, *ACS Nano*, 2024, **18**, 21651–21684.

8 G. Nazir, A. Rehman, J.-H. Lee, C.-H. Kim, J. Gautam, K. Heo, S. Hussain, M. Ikram, A. A. AlObaid, S.-Y. Lee and S.-J. Park, A Review of Rechargeable Zinc–Air Batteries: Recent Progress and Future Perspectives, *Nano-Micro Lett.*, 2024, **16**, 138.

9 T. An, X. Ge, N. N. Tham, A. Sumboja, Z. Liu and Y. Zong, Facile One-Pot Synthesis of CoFe Alloy Nanoparticles Decorated N-Doped Carbon for High-Performance Rechargeable Zinc–Air Battery Stacks, *ACS Sustainable Chem. Eng.*, 2018, **6**, 7743–7751.

10 X. Han, X. Yu and H. S. Park, Recent advances in trifunctional electrocatalysts for Zn–air batteries and water splitting, *Mater. Chem. Front.*, 2024, **8**, 1536–1562.

11 D. W. Kim, J. H. Choi, S. Cho, K.-H. Kim and J. K. Kang, High-Valent NiFe Core/Porous Pyridinic N-Doped Graphitic Carbon Shell as a Robust Oxygen Electrocatalyst for High Performance in Zn–Air Batteries, *ACS Appl. Mater. Interfaces*, 2025, **17**, 32469–32478.

12 Z.-F. Huang, J. Wang, Y. Peng, C.-Y. Jung, A. Fisher and X. Wang, Design of efficient bifunctional oxygen reduction/evolution electrocatalyst: recent advances and perspectives, *Adv. Energy Mater.*, 2017, **7**, 1700544.

13 Krishankant, Aashi, Z. Ahmed, S. Alagar, A. Gaur, R. Kaur and V. Bagchi, Nano-interfaced tungsten oxide decorated on layered double hydroxides for the oxygen evolution reaction, *Sustainable Energy Fuels*, 2022, **6**, 4429–4436.

14 C.-X. Zhao, J.-N. Liu, J. Wang, D. Ren, B.-Q. Li and Q. Zhang, Recent advances of noble-metal-free bifunctional oxygen reduction and evolution electrocatalysts, *Chem. Soc. Rev.*, 2021, **50**, 7745–7778.

15 Y. Li, L. Zhang, Y. Han, W. Ji, Z. Liu, B. Wang, S. Zhao, X. Wu, L. Zhang and R. Zhang, Interface engineering of bifunctional oxygen electrocatalysts for rechargeable Zn–air batteries, *Mater. Chem. Front.*, 2023, **7**, 4281–4303.

16 S. Rasaily, S. Chettri, D. Sharma, K. Baruah, R. Dewan, S. Tamang and A. Pariyar, MOF-Derived Ni/NiO-C Nanocomposites as Bifunctional Electrocatalysts Capable of Driving Both ORR and OER, *Inorg. Chem.*, 2024, **63**, 17846–17855.

17 Y. Chen, G. Wang, J. Li, T. He, Y. Zhang, H. Zhang and Y.-N. Liu, Recent advances in bifunctional carbon-based single-atom electrocatalysts for rechargeable zinc–air batteries, *Green Chem.*, 2025, **27**, 293–324.

18 Aashi, A. Chaudhuri, Krishankant, V. Pundir, Z. Ahmed, C. Bera, C. Bakli and V. Bagchi, Unveiling the Potential of Metal–Organic Frameworks: Nucleation-Induced Strain Activating Electrocatalytic Water Splitting, *ACS Sustainable Chem. Eng.*, 2024, **12**, 14276–14287.

19 Q. Zhou, S. Zhang, G. Zhou, H. Pang, M. Zhang, L. Xu, K. Sun, Y. Tang and K. Huang, Interfacial engineering of CoN/Co_3O_4 heterostructured hollow nanoparticles embedded in N-doped carbon nanowires as a bifunctional oxygen electrocatalyst for rechargeable liquid and flexible all-solid-state Zn–air batteries, *Small*, 2023, **19**, 2301324.

20 L. Peng, L. Shang, T. Zhang and G. I. Waterhouse, Recent advances in the development of single-atom catalysts for oxygen electrocatalysis and zinc–air batteries, *Adv. Energy Mater.*, 2020, **10**, 2003018.

21 J. Sun, Z. Wang and J. Guan, Single-atom Ce catalysts for rechargeable Zn–air batteries, *Mater. Chem. Front.*, 2025, **9**, 1574–1580.

22 Q. Yang, R. Liu, Y. Pan, Z. Cao, J. Zuo, F. Qiu, J. Yu, H. Song, Z. Ye and S. Zhang, Ultrahigh-Loaded Fe Single Atoms and Fe_3C Nanoparticle Catalysts as Air Cathodes for High-Performance Zn–Air Batteries, *ACS Appl. Mater. Interfaces*, 2023, **15**, 5720–5731.

23 C. Z. Loyola, G. Abarca, S. Ureta-Zañartu, C. Aliaga, J. H. Zagal, M. T. Sougrati, F. Jaouen, W. Orellana and F. Tasca, Insights into the electronic structure of Fe pentacoordinated complexes. Spectroscopic examination and electrochemical analysis for the oxygen reduction and oxygen evolution reactions, *J. Mater. Chem. A*, 2021, **9**, 23802–23816.

24 Y. Kumar, S. Akula, J. Kozlova, A. Kikas, J. Aruväli, M. Käärik, A. Treshchalov, J. Leis, V. Kisand, K. Kukli, E. Kibena-Põldsepp and K. Tammeveski, Zinc-assisted synthesis of polymer framework-based atomically dispersed bimetal catalysts for efficient oxygen electrocatalysis in rechargeable zinc–air batteries, *J. Energy Storage*, 2024, **86**, 111164.

25 X. Yu, S. Lai, S. Xin, S. Chen, X. Zhang, X. She, T. Zhan, X. Zhao and D. Yang, Coupling of iron phthalocyanine at carbon defect site *via* π–π stacking for enhanced oxygen reduction reaction, *Appl. Catal., B*, 2021, **280**, 119437.

26 Y. Luo, Y. Chen, Y. Xue, J. Chen, G. Wang, R. Wang, M. Yu and J. Zhang, Electronic Structure Regulation of Iron Phthalocyanine Induced by Anchoring on Heteroatom-Doping Carbon Sphere for Efficient Oxygen Reduction Reaction and Al–Air Battery, *Small*, 2022, **18**, 2105594.

27 Y. Jiang, Y. Lu, X. Lv, D. Han, Q. Zhang, L. Niu and W. Chen, Enhanced Catalytic Performance of Pt-Free Iron Phthalocyanine by Graphene Support for Efficient Oxygen Reduction Reaction, *ACS Catal.*, 2013, **3**, 1263–1271.

28 H. Zhang, Z. Zhang, Z. Zhang, Y. Li, Y. Hou, P. Liu, B. Xu, H. Zhang, Y. Liu and J. Guo, Highly dispersed ultrasmall iron phthalocyanine molecule clusters confined by mesopore-rich N-doped hollow carbon nanospheres for efficient oxygen reduction reaction and Zn–air battery, *Chem. Eng. J.*, 2023, **469**, 143996.

29 S. Yang, Y. Yu, X. Gao, Z. Zhang and F. Wang, Recent advances in electrocatalysis with phthalocyanines, *Chem. Soc. Rev.*, 2021, **50**, 12985–13011.

30 L. Scarpetta-Pizo, I. Ponce, R. Onate, S. del Valle, Z. Ahmed, K. Tammeveski and J. H. Zagal, Linear free-energy

relationships. Reactivity descriptors and guidelines based on ligand parametrization for electroreduction of O_2 catalyzed by metallophthalocyanines and metalloporphyrins, *J. Porphyrins phthalocyanines*, 2025, **29**, 304–321.

31 J. Sheng, S. Sun, G. Jia, S. Zhu and Y. Li, Doping Effect on Mesoporous Carbon-Supported Single-Site Bifunctional Catalyst for Zinc–Air Batteries, *ACS Nano*, 2022, **16**, 15994–16002.

32 L. Ran, Y. Xu, X. Zhu, S. Chen and X. Qiu, Mn Single-Atom Tuning Fe–N–C Catalyst Enables Highly Efficient and Durable Oxygen Electrocatalysis and Zinc–Air Batteries, *ACS Nano*, 2024, **18**, 750–760.

33 X. Chen, D. Yue, X. Yu, Y. Chen, X. Chen, H. Wang, Q. Li and Z. Ma, Microenvironment Tailoring of NiCo Alloys Coupled with FePc as Efficient Bifunctional Catalysts for High-Rate Zn–Air Batteries, *Langmuir*, 2024, **40**, 17038–17048.

34 J. Wang, H. Hu, H. Zhang, J. Zhao, X. Li, Z. Song, J. Ding, Y. Deng, X. Han and W. Hu, Regulating the Catalytically Active Sites in Low-Cost and Earth-Abundant 3d Transition-Metal-Based Electrode Materials for High-Performance Zinc–Air Batteries, *Energy Fuels*, 2021, **35**, 6483–6503.

35 H. Hu, Y. Xie, F. M. D. Kazim, K. Qu, M. Li, Z. Xu and Z. Yang, Synergetic FeCo nanorods embedded in nitrogen-doped carbon nanotubes with abundant metal–NCNT heterointerfaces as efficient air electrocatalysts for rechargeable zinc–air batteries, *Sustainable Energy Fuels*, 2020, **4**, 5188–5194.

36 S. Zhang, J. Yang, L. Yang, T. Yang, Y. Liu, L. Zhou, Z. Xu, X. Zhou and J. Tang, Boosting ORR/OER bifunctional electrocatalysis by promoting electronic redistribution of Fe–N–C on CoFe–FeNC for ultra-long rechargeable Zn–air batteries, *Appl. Catal., B*, 2024, **359**, 124485.

37 S. Ding, L. He, L. Fang, Y. Zhu, T. Li, Z. Lyu, D. Du, Y. Lin and J.-C. Li, Carbon-nanotube-bridging strategy for integrating single Fe atoms and NiCo nanoparticles in a bifunctional oxygen electrocatalyst toward high-efficiency and long-life rechargeable zinc–air batteries, *Adv. Energy Mater.*, 2022, **12**, 2202984.

38 Z. Ahmed, S. Akula, J. Kozlova, H.-M. Piirsoo, K. Kukli, A. Kikas, V. Kisand, M. Käärik, J. Leis, A. Treshchalov, J. Aruväli and K. Tammeveski, Hybrid high-performance oxygen reduction reaction Fe–N–C electrocatalyst for anion exchange membrane fuel cells, *Int. J. Hydrogen Energy*, 2024, **62**, 849–858.

39 Y. Li, Y. Guo, N. Ebato, Y. Yamauchi and Y. Sugahara, Hierarchically Meso-Macroporous N-Doped Carbon Embedded with CoFe-Based Composite for the Oxygen Reduction Reaction, *ACS Electrochem.*, 2025, **1**, 407–418.

40 M. Mooste, Z. Ahmed, P. Kapitulskis, R. Ivanov, A. Treshchalov, H.-M. Piirsoo, A. Kikas, V. Kisand, K. Kukli, I. Hussainova and K. Tammeveski, Bifunctional oxygen electrocatalyst based on Fe, Co, and nitrogen co-doped graphene-coated alumina nanofibers for Zn–air battery air electrode, *Appl. Surf. Sci.*, 2024, **660**, 160024.

41 Z. Ahmed, J. Kozlova, K. Kukli, A. Kikas, V. Kisand, A. Treshchalov, M. Käärik, J. Leis, J. Aruväli and K. Tammeveski, Boosting bifunctional oxygen electrocatalysis by integrating Fe–Nx moieties and FeNi nanoparticles for highly efficient and long-life rechargeable zinc–air batteries, *Sustainable Energy Fuels*, 2025, **9**, 2098–2108.

42 J. Yang, J. Tao, T. Isomura, H. Yanagi, I. Moriguchi and N. Nakashima, A comparative study of iron phthalocyanine electrocatalysts supported on different nanocarbons for oxygen reduction reaction, *Carbon*, 2019, **145**, 565–571.

43 R. Kumar, M. Mooste, Z. Ahmed, S. Akula, I. Zekker, M. Marandi, M. Käärik, J. Leis, A. Kikas, A. Treshchalov, M. Otsus, J. Aruväli, V. Kisand, A. Tamm and K. Tammeveski, Highly active ZIF-8@CNT composite catalysts as cathode materials for anion exchange membrane fuel cells, *Ind. Chem. Mater.*, 2023, **1**, 526–541.

44 X. Zhang, R. Zheng, Q. Chang, Z. Ma and Z. Yang, Regulating the frontier orbital of iron phthalocyanine with nitrogen doped carbon nanosheets for improving oxygen reduction activity, *Nanoscale*, 2024, **16**, 8036–8045.

45 K.-M. Zhao, S. Liu, Y.-Y. Li, X. Wei, G. Ye, W. Zhu, Y. Su, J. Wang, H. Liu and Z. He, Insight into the mechanism of axial ligands regulating the catalytic activity of Fe–N_4 sites for oxygen reduction reaction, *Adv. Energy Mater.*, 2022, **12**, 2103588.

46 Z. Mei, S. Cai, G. Zhao, X. Zou, Y. Fu, J. Jiang, Q. An, M. Li, T. Liu and H. Guo, Boosting the ORR active and Zn–air battery performance through ameliorating the coordination environment of iron phthalocyanine, *Chem. Eng. J.*, 2022, **430**, 132691.

47 Z. Li, X. Wu, X. Jiang, B. Shen, Z. Teng, D. Sun, G. Fu and Y. Tang, Surface carbon layer controllable Ni_3Fe particles confined in hierarchical N-doped carbon framework boosting oxygen evolution reaction, *Adv. Powder Mater.*, 2022, **1**, 100020.

48 M. Zhong, N. Song, C. Li, C. Wang, W. Chen and X. Lu, Controllable growth of Fe-doped NiS_2 on NiFe-carbon nanofibers for boosting oxygen evolution reaction, *J. Colloid Interface Sci.*, 2022, **614**, 556–565.

49 Y. Li, H. Zhang, M. Jiang, Q. Zhang, P. He and X. Sun, 3D self-supported Fe-doped Ni_2P nanosheet arrays as bifunctional catalysts for overall water splitting, *Adv. Funct. Mater.*, 2017, **27**, 1702513.

50 J. Zhao, Q. Li, Q. Zhang and R. Liu, Carbon tube-graphene heterostructure with different N-doping configurations induces an electrochemically active-active interface for efficient oxygen electrocatalysis, *Chem. Eng. J.*, 2022, **431**, 133730.

51 C. Du, P. Li, Z. Zhuang, Z. Fang, S. He, L. Feng and W. Chen, Highly porous nanostructures: Rational fabrication and promising application in energy electrocatalysis, *Coord. Chem. Rev.*, 2022, **466**, 214604.

52 Z. Yuan, M. Fan, Y. Wang, Y. Cheng and H. Zhang, N, S-Codoped Porous Carbon with Densely Edge Structure for Oxygen Reduction Reaction and Zinc–Air Battery, *ACS Appl. Energy Mater.*, 2024, **7**, 1598–1605.

53 Y. Wang, X.-Y. Zhang, H. He, J.-J. Chen and B. Liu, Ordered Mesoporous High-Entropy Intermetallics for Efficient Oxygen Reduction Electrocatalysis, *Adv. Energy Mater.*, 2024, **14**, 2303923.

54 A. J. Bard and L. R. Faulkner, *Electrochemical methods: fundamentals and applications*, Wiley, New York, 2nd edn, 2001.
55 A. Ch Lazanas and M. I. Prodromidis, Electrochemical Impedance Spectroscopy—A Tutorial, *ACS Meas. Sci. Au*, 2023, **3**, 162–193.
56 Z. Mei, S. Cai, G. Zhao, Q. Jing, X. Sheng, J. Jiang and H. Guo, Understanding electronic configurarions and coordination environment for enhanced ORR process and improved Zn–air battery performance, *Energy Storage Mater.*, 2022, **50**, 12–20.
57 G. Bae, H. Kim, H. Choi, P. Jeong, D. H. Kim, H. C. Kwon, K.-S. Lee, M. Choi, H.-S. Oh, F. Jaouen and C. H. Choi, Quantification of Active Site Density and Turnover Frequency: From Single-Atom Metal to Nanoparticle Electrocatalysts, *JACS Au*, 2021, **1**, 586–597.
58 R. Nandan, H. R. Devi, R. Kumar, A. K. Singh, C. Srivastava and K. K. Nanda, Inner Sphere Electron Transfer Promotion on Homogeneously Dispersed Fe–N*x* Centers for Energy-Efficient Oxygen Reduction Reaction, *ACS Appl. Mater. Interfaces*, 2020, **12**, 36026–36039.
59 R. Kumar, M. Mooste, Z. Ahmed, I. Zekker, M. Käärik, M. Marandi, J. Leis, A. Kikas, M. Otsus, A. Treshchalov, J. Aruväli, M. Jaagura, V. Kisand, A. Tamm and K. Tammeveski, Catalyzing oxygen reduction by morphologically engineered ZIF-derived carbon composite catalysts in dual-chamber microbial fuel cells, *J. Environ. Chem. Eng.*, 2024, **12**, 112242.
60 X. Wang, S. Xi, P. Huang, Y. Du, H. Zhong, Q. Wang, A. Borgna, Y.-W. Zhang, Z. Wang, H. Wang, Z. G. Yu, W. S. V. Lee and J. Xue, Pivotal role of reversible NiO6 geometric conversion in oxygen evolution, *Nature*, 2022, **611**, 702–708.
61 A. Pandikassala, M. Kurian, P. K. Gangadharan, A. Torris and S. Kurungot, Advanced 3D Network of N-Doped Graphitic Carbon with FeNi Alloy Embedding for High-Performance Rechargeable Zn–Air Batteries, *Adv. Sustainable Syst.*, 2024, **8**, 2400012.
62 M. P. Clark, M. Xiong, K. Cadien and D. G. Ivey, High Performance Oxygen Reduction/Evolution Electrodes for Zinc–Air Batteries Prepared by Atomic Layer Deposition of MnO_x, *ACS Appl. Energy Mater.*, 2020, **3**, 603–613.
63 N. Shang, K. Wang, M. Wei, Y. Zuo, P. Zhang, H. Wang, Z. Chen and P. Pei, Challenges for large scale applications of rechargeable Zn–air batteries, *J. Mater. Chem. A*, 2022, **10**, 16369–16389.
64 Q. Wang, S. Kaushik, X. Xiao and Q. Xu, Sustainable zinc–air battery chemistry: advances, challenges and prospects, *Chem. Soc. Rev.*, 2023, **52**, 6139–6190.
65 P. Zhang, M. Wei, K. Wang, H. Wang, Y. Zuo and M. Zhang, Performance optimization of zinc–air batteries *via* nanomaterials, *Energy Storage Mater.*, 2025, **75**, 104109.

